



1 **Two superimposed cold and fresh anomalies enhanced Irminger Sea**
2 **deep convection in 2016 – 2018**

3

4 Patricia ZUNINO¹, Herlé MERCIER² and Virginie THIERRY³.

5 1 Altran Technologies, Technopôle Brest Iroise, Site du Vernis , 300 rue Pierre Rivoalon, 29200 Brest,
6 France

7 2 CNRS, University of Brest, IRD, Ifremer, Laboratoire d'Océanographie Physique et Spatiale (LOPS),
8 IUEM, ZI de la pointe du diable, CS 10070 - 29280 Plouzané, France

9 3 Ifremer, University of Brest, CNRS, IRD, Laboratoire d'Océanographie Physique et Spatiale (LOPS),
10 IUEM, ZI de la pointe du diable, CS 10070 - 29280 Plouzané, France

11

12 Corresponding author: patricia.zuninorodriguez@altran.fr

13

14

15

16

17

18

19

20

21

22

23

24

25

26

27

28

29

30

31

32

33

34

35

36

37

38

39

40

41



42 **ABSTRACT**

43 While Earth system models project a reduction, or even a shut-down, of deep convection in the
44 North Atlantic Ocean in response to anthropogenic forcing, deep convection returned to the Irminger
45 Sea in 2008 and occurred several times since then to reach exceptional depths > 1,500 m in 2015 and
46 2016. In this context, we used Argo data to show that deep convection persisted in the Irminger Sea
47 during two additional years in 2017 and 2018 with maximum convection depth > 1,300 m. In this
48 article, we investigate the respective roles of air-sea flux and preconditioning of the water column to
49 explain this exceptional 4-year persistence of deep convection; we quantified them in terms of
50 buoyancy and analyzed both the heat and freshwater components. Contrary to the very negative air-
51 sea buoyancy flux that was observed during winter 2015, the buoyancy fluxes over the Irminger Sea
52 during winters 2016, 2017 and 2018 were close to climatological average. We estimated the
53 preconditioning of the water column as the buoyancy that needs to be removed (B) from the end of
54 summer water column to homogenize the water column down to a given depth. B was lower for
55 winters 2016 – 2018 than for the mean 2008 – 2015, including a vanishing stratification from 600 m
56 down to ~1,300 m. It means that less air-sea buoyancy loss was necessary to reach a given
57 convection depth than in the mean and once convection reached 600 m little additional buoyancy
58 loss was needed to homogenize the water column down to 1,300 m. We showed that the decrease in
59 B was due to the combined effects of a cooling of the intermediate water (200 – 800 m) and a
60 decrease in salinity in the 1,200 – 1,400 m layer. This favorable preconditioning permitted the very
61 deep convection observed in 2016 – 2018 despite the atmospheric forcing was close to the
62 climatological average.

63

64

65

66

67

68

69



70 1. INTRODUCTION

71 The physical and biogeochemical properties of the oceans are experiencing unprecedented changes
72 as a result of the human activities (IPCC, 2013). For this reason, a challenge for the oceanographic
73 community is to disentangle the natural and anthropogenic components of the ocean variability.
74 Under Climate Change scenarios, Earth system models predict a warmer climate, an increase in
75 freshwater flux into the ocean due to ice melting (Bamber et al., 2018)), a slow-down of the
76 Meridional Overturning Circulation (Rahmstorf et al., 2015), and a reduction or shut-down of deep
77 convection in the North Atlantic (Brodeau & Koenigk, 2016). In this paper, we study the recent
78 evolution of deep convection in the northern North Atlantic.

79 Deep convection is the result of a process by which surface waters lose buoyancy due to
80 atmospheric forcing and sink into the interior ocean. It occurs only where specific conditions are met
81 including large air-sea buoyancy loss and favorable preconditioning (i.e. low stratification of the
82 water column) (Marshall & Schott, 1999). In the Subpolar North Atlantic (SPNA), deep convection
83 takes place in the Labrador Sea and in the Irminger Sea (Kieke & Yashayaev, 2015; Pickart et al. 2003)
84 connecting the upper and lower limbs of the Meridional Overturning Circulation (MOC) and
85 transferring climate change signals from the surface to the ocean interior.

86 The observation and description of deep convection is difficult because deep convection happens at
87 very short space and time scales (Marshall & Schott, 1999) and during periods of severe weather
88 conditions. The onset of the Argo program (<http://www.argo.net/>) at the beginning of the 2000s, has
89 considerably increased the availability of oceanographic data. Although the sampling characteristics
90 of Argo are not adequate to observe the smaller scales associated with the process itself, this dataset
91 allowed the description of the overall intensity of the event, and the properties of the water masses
92 formed in the winter mixed layer (e.g., Yashayaev and Loder, 2017). The challenge now is to evaluate
93 how deep convection could evolve under climate change.

94 In the Labrador Sea, deep convection occurs almost every year, yet with different intensity (e.g.,
95 Yashayaev and Clarke, 2008; Kieke and Yashayaev, 2015). In the Irminger Sea, Argo and moorings
96 data showed that deep convection happened in the Irminger Sea during winters 2008, 2009, 2012,
97 2015 and 2016 (Våge et al., 2009; de Jong et al., 2012; Piron et al. 2015; de Jong & de Steur, 2016;
98 Piron et al. 2017; de Jong et al., 2018). Excluding the winter 2009 when the event was possible
99 thanks to a favorable preconditioning set the winter before (de Jong et al. 2012), all events coincided
100 with strong atmospheric-forcing (air-sea heat loss). Prior to 2008, only few deep convection events
101 were reported because the mechanisms leading to it were not favorable (Centurioni and Gould,



102 2004) and because the observing system was not adequate (Bacon, 1997; Pickart et al., 2003).
103 Nevertheless, the hydrographic properties from the 1990s suggested that deep convection reached
104 as deep as 1,500 m in the Irminger Sea during winters 1994 and 1995 (Pickart et al., 2003).

105 The convection of winter 2015 was the deepest observed in the Irminger Sea since the beginning of
106 the 21st century (de Jong et al., 2016; Piron et al., 2016). In this work, we show that deep convection
107 also happened each winter in the Irminger Sea during the period 2016 – 2018. We investigate the
108 respective role of atmospheric forcing and preconditioning in setting the convection intensity. We
109 evaluate them in terms of air-sea buoyancy flux and buoyancy content and, for the first time to our
110 knowledge in this region, we disentangle the relative contribution of salinity and temperature
111 anomalies to the preconditioning. The paper is organized as follow. The data are described in Sect. 2.
112 The methodology is explained in Sect. 3. We expose our results in Sect. 4 and discuss them in Sect. 5.
113 Conclusions are listed in Sect. 6.

114

115 2. DATA

116 We used temperature (T), salinity (S) and pressure (P) data measured by Argo floats north of 55°N in
117 the Atlantic Ocean. These data were collected by the International Argo program
118 (<http://www.argo.ucsd.edu/>, <http://www.jcommops.org/>) and downloaded from the Coriolis Data
119 Center (<http://www.coriolis.eu.org/>). Only data flagged as good (quality Control < 3, Argo Data
120 Management Team, 2017) were considered in our analysis. Potential temperature (θ), density (ρ)
121 and potential density anomaly referenced to the surface and 1000 dbar (σ_0 and σ_1 , respectively) were
122 estimated from T, S and P data using TEOS-10 (<http://www.teos-10.org/>). As in Zunino et al. (2017),

123 we define freshwater as: $FW = \frac{35-S}{35}$.

124 We used two different gridded products of ocean T and S: EN4 and ISAS. ISAS (Gaillard et al., 2016;
125 Kolodziejczyk et al., 2017) is produced by optimal interpolation of *in situ* data. It provides monthly
126 fields, at 152 depth levels, at 0.5° resolution, from 2002 to 2015. Near real time data are also
127 available for 2016 and 2018. EN4 (Good et al., 2013) is an optimal interpolation of *in situ* data; it
128 provides monthly T and S at 1° spatial resolution and at 42 depth levels, for the period 1900 to
129 present.

130 Net air-sea heat flux (Q), evaporation (E), precipitation (P), wind stress (τ_x and τ_y) and sea surface
131 temperature (SST) data were obtained from ERA-Interim reanalysis (Dee et al., 2011). ERA-Interim
132 provides data with a time resolution of 12h and a spatial resolution of 0.75°, respectively. The air-sea
133 freshwater flux (FWF) was estimated as E - P.



134 We used monthly Absolute Dynamic Topographic (ADT), which was computed from the daily 0.25° -
135 resolution ADT data provided by CMEMS (Copernicus Marine and Environment Monitoring Service,
136 <http://www.marine.copernicus.eu>).

137

138 3. METHODS

139 3.1 Quantification of the deep convection

140 In order to characterize the convection in the Irminger Sea and Labrador Sea in winters 2015-2018,
141 we estimated the mixed layer depths (MLD) for all Argo profiles collected in the SPNA north of 55°N
142 from 1st January to 30th April of each year (Fig. 1). Following Piron et al. (2016), the MLD was
143 estimated by the threshold method (de Boyer Montégut et al., 2004) and the split and merge
144 method (Thomson and Fine, 2003) complemented by visual inspection of the vertical profiles of ρ
145 when the two estimates differed. In this paper, deep convection is characterized by profiles with
146 MLD deeper than 700m (colored big points in Fig. 1) because it is the minimum depth that should be
147 reached for Labrador Sea Water (LSW) renewal (Yashayaev et al., 2007; Piron et al. 2016).

148 The winter MLD and the associated θ , S and ρ properties were examined for the Labrador Sea and
149 the Irminger Sea, separately. We used 48°W as the limit between the Irminger Sea and the Labrador
150 Sea. We computed the maximum MLD and the MLD third quartile (Q_3) (we only used MLD greater
151 than 700m for the computation of Q_3). Q_3 is the MLD value that is exceeded by 25% of the profiles
152 and is equivalent to the aggregate maximum depth of convection defined by Yashayaev and Loder
153 (2016). The properties (ρ , θ and S) of the mixed layers formed each winter were defined as the
154 vertical mean from 200 m to the MLD of the n profiles with MLD deeper than 700 m.

155 3.2. Time series of atmospheric forcing

156 The air-sea buoyancy flux (B_{surf}) was calculated as the sum of the contributions of Q and FWF (Gill,
157 1982; Billheimer & Talley, 2013). It reads:

$$158 \quad B_{surf} = \frac{\alpha \cdot g}{\rho_0 \cdot c_p} \cdot Q - \beta \cdot g \cdot SSS \cdot FWF \quad \text{Eq. (1)}$$

159 Where α and β are the coefficients of thermal and saline expansions, respectively, estimated from
160 surface T and S . The gravitational acceleration g is equal to 9.8 m s^{-2} , the reference density of sea
161 water ρ_0 is equal to 1026 kg m^{-3} and heat capacity of sea water c_p is equal to $3990 \text{ J kg}^{-1} \text{ °C}^{-1}$. SSS is
162 the sea surface salinity. Q and FWF are in W m^{-2} and m s^{-1} , respectively.



163 For easy comparison with previous results that only considered the heat component of the total air-
164 sea flux (e.g. Yashayaev & Loder, 2017; Piron et al. 2017; Rhein et al., 2017), B_{surf} , in $m^2 s^{-3}$, was
165 converted to $W m^{-2}$ following Eq. (2) and noted B_{surf}^*

$$166 \quad B_{surf}^* = \frac{\rho_0 \cdot c_p}{g \cdot \alpha} \cdot B_{surf} \quad \text{Eq. (2)}$$

167 The FWF was also converted to $W m^{-2}$ using:

$$168 \quad FWF^* = FWF \cdot \beta \cdot SSS \cdot \frac{\rho_0 \cdot c_p}{\alpha} \quad \text{Eq. (3)}$$

169 We also computed the horizontal Ekman buoyancy flux (BF_{ek}), and their components the horizontal
170 Ekman heat flux (HF_{ek}) and the horizontal Ekman salt flux (SF_{ek}), for which $BF_{ek} = SF_{ek} - HF_{ek}$.

$$171 \quad BF_{ek} = -g \cdot (U_e \partial_x SSD + V_e \partial_y SSD) \cdot \frac{c_p}{\alpha \cdot g} \quad \text{Eq. (4)}$$

$$172 \quad HF_{ek} = -(U_e \partial_x SST + V_e \partial_y SST) \cdot \rho_0 \cdot c_p \quad \text{Eq. (5)}$$

$$173 \quad SF_{ek} = -(U_e \partial_x SSS + V_e \partial_y SSS) \cdot \frac{\beta \cdot \rho_0 \cdot c_p}{\alpha} \quad \text{Eq. (6)}$$

174 where U_e and V_e are the eastward and westward components of the Ekman horizontal transport
175 estimated from the wind stress meridional and zonal components. SSD, SST and SSS are ρ , T and S at
176 the surface of the ocean. The factors on the right of equations are used to obtain BF_{ek} , HF_{ek} and SF_{ek} in
177 $J s^{-1} m^{-2}$. Because ERA-Interim does not supply SSD or SSS, the monthly S at 5 m depth from EN4 were
178 interpolated on the same time and space grid as the air-sea fluxes from ERA-Interim (12h and 0.75° ,
179 respectively). SSD was estimated from SST of ERA-Interim and interpolated S of EN4. Data at points
180 shallower than 1000 m were excluded from the analysis to avoid regions covered by sea-ice.

181 Following Piron et al. (2016), the time series of atmospheric forcing were estimated for the Irminger
182 Sea and the Labrador Sea as follows. First, the gridded air-sea flux data and the horizontal Ekman
183 fluxes were averaged over the region, pink and cyan boxes in Fig. 1 for the Irminger Sea and Labrador
184 Sea, respectively. The boxes, which are representative of the convection regions, were defined to
185 include most of Argo profiles with MLD deeper than 700 m and the minimum of the monthly ADT for
186 either the Irminger Sea or the Labrador Sea. Second, we estimated the accumulated fluxes from 1
187 September to 31 August the year after. Finally, we computed the time series of the anomalies of the
188 accumulated fluxes from 1 September to 31 August with respect to the 1993 – 2016 mean.

189 Finally, in order to quantify the intensity of the atmospheric forcing over the winter, we computed
190 estimates of air-sea fluxes accumulated from 1 September to 31 March the year after. The associated



191 errors were calculated by Monte Carlo simulation as the standard deviation of 50 estimates of Q,
 192 FWF and B_{surf} perturbed by one standard deviation of their spatial mean. The error amounted to 0.05
 193 J m^2 , 0.04 and 0.03 J m^2 for B_{surf}^* , Q and FWF*, respectively. The error of the horizontal Ekman
 194 transport was also estimated by Monte Carlo simulation and amounted to 0.04 J m^2 .

195 3.3. Preconditioning of the water column

196 The preconditioning of the water column was evaluated in terms of buoyancy that has to be
 197 removed ($B(z_i)$) to the late summer density profile to homogenize it down to a depth z_i . It reads:

$$198 \quad B(z_i) = \frac{g}{\rho_0} * \sigma_0(z_i) * z_i - \frac{g}{\rho_0} \int_{z_i}^0 \sigma_0(z) dz \quad \text{Eq. (7)}$$

199 $\sigma_0(z)$ is the vertical profile of potential density anomaly estimated from the profiles of T and S
 200 measured by Argo floats in September in the given region (pink or cyan box in Fig. 1).

201 Following Schmidt and Send (2007), we split B into a temperature (B_θ) and salinity (B_S) term as:

$$202 \quad B_\theta(z_i) = -(g * \alpha * \theta(z_i) * z_i - g * \alpha * \int_{z_i}^0 \theta(z) dz) \quad \text{Eq. (8)}$$

$$203 \quad B_S(z_i) = g * \beta * S(z_i) * z_i - g * \beta * \int_{z_i}^0 S(z) dz \quad \text{Eq. (9)}$$

204 In order to compare the B with the heat to be removed and/or air-sea heat fluxes, the buoyancy
 205 results in $\text{m}^2 \text{s}^{-2}$ were converted to J m^{-2} .

206 B , B_θ and B_S were estimated for a given year from the mean of all September profiles of B , B_θ and
 207 B_S . The associated errors were estimated as $\text{std}(B)/\sqrt{n}$, where n is the number of profiles used to
 208 compute the September mean values.

209

210 4. RESULTS

211 4.1. Intensity of deep convection and properties of newly formed LSW

212 We examine the time-evolution of the Irminger Sea winter mixed layer since the exceptional
 213 convection event of winter 2015 (W2015 hereinafter) (Table 1 and Fig. 3). In W2015 we recorded a
 214 maximum MLD of 1,715 m south of Cape Farewell (Fig. 1a), in line with Piron et al. (2017). The
 215 maximum MLD of 1,575 m observed for W2016 (Fig. 1b) is compatible with the MLD > 1,500 m
 216 observed in a mooring array in the central Irminger Sea by de Jong et al. (2018). We additionally
 217 showed that for both winters Q3 was about 1300 m (Table 1). Now, we describe the convection of



218 W2017 and W2018. In W2017, deep convection was defined from four Argo profiles in the Irminger
219 Sea (see Fig. 1c and Fig. 2a-c). The maximum MLD of 1,400 m was observed on 16th March 2017 at
220 56.65°N – 42.30°W. The aggregate maximum depth of convection Q3 coincided with the maximum
221 MLD because the estimates are based on only four profiles. In W2018, ten profiles showed MLD
222 deeper than 700 m in the Irminger Sea (Fig. 1d, 2d-f). The maximum MLD of 1,300 m was observed
223 on 24 February at 58.12°N, 41.84°W. The aggregate maximum depth of convection Q3 was 1,100 m.
224 Float 5903102, which was localized South of Cape Farewell, did not profile deeper than 1,100 m in
225 any of its six cycles (see Fig. 2d-f); it is therefore possible that the MLD was deeper than 1,100 m in
226 these profiles. Excluding the data of Float 5903102, the aggregate maximum depth of convection Q3
227 is 1,300 m. These results reveal that convection deeper than 1,300 m occurred during four
228 consecutive winters in the Irminger Sea.

229 The properties (σ_0 , S and θ) of the end of winter mixed layer were estimated for the four winters
230 (Table 1 and Fig. 3). We observed that, between W2015 and W2018, the water mass formed by deep
231 convection significantly densified and cooled by 0.019 kg m⁻³ and 0.306°C, respectively (see Table 1).

232 In the Labrador Sea, Q3 increased from 2015 to 2018 (see Table 1). Deep convection observed in the
233 Labrador Sea in W2018 was the most intense since the beginning of the Argo era (see Fig. 2c in
234 Yashayaev & Loder, 2016). From W2015 to W2018, newly formed LSW cooled, salted and densified
235 by 0.134°C, 0.013 and 0.023 kg m⁻³, respectively (Table 1).

236 The water mass formed in the Irminger Sea is warmer and saltier than that formed in the Labrador
237 Sea (Fig. 3); the exception is in W2018 when the characteristics of the water masses formed in each
238 of the basins are very similar. The deep convection in the Irminger Sea is always shallower than in the
239 Labrador Sea. Both results are discussed later in Sect. 5.

240 4.2. Analysis of the atmospheric forcing in the Irminger Sea

241 The seasonal cycles of B_{surf}^* and Q are in phase and of the same order of magnitude, while the FWF*
242 is positive and one order of magnitude lower than Q and does not present a seasonal cycle (Fig. S1).
243 The means (1993 – 2018) of the cumulative sums from 1 September to 31 March of Q, FWF* and
244 B_{surf}^* estimated over the Irminger box (Fig. 1) are $-2.52 \pm 0.43 \times 10^9 \text{ J m}^{-2}$, $0.31 \pm 0.11 \times 10^9 \text{ J m}^{-2}$ and
245 $-2.26 \pm 0.51 \times 10^9 \text{ J m}^{-2}$, respectively. Despite B_{surf}^* is mainly explained by Q, the accumulated FWF*
246 amounts to ~10 % of the accumulated Q with opposite sign. The atmospheric forcing estimated in
247 terms of buoyancy is therefore 10% lower on average than when estimated in terms of heat.



248 Piron et al. (2016) found that “the wind stress led to an Ekman-induced heat loss that reinforced by
249 about 10% the heat loss induced by the net air-sea heat fluxes”. Here, we considered the buoyancy
250 flux induced by the Ekman response to the wind stress and we estimated the buoyancy, heat and salt
251 Ekman fluxes (BF_{ek} , HF_{ek} and SF_{ek}). The means (1993 - 2018) of the accumulated BF_{ek} , HF_{ek} and SF_{ek}
252 from 1 September to 31 March amount to $-0.0004 \pm 0.04 \times 10^9 \text{ J m}^{-2}$, $0.0446 \pm 0.04 \times 10^9 \text{ J m}^{-2}$, and
253 $0.0626 \pm 0.04 \times 10^9 \text{ J m}^{-2}$, respectively. So, on average, HF_{ek} and SF_{ek} compensate each other resulting
254 in an almost zero $\text{J m}^{-2} BF_{ek}$. However, for particular years with strong wind stress as it was the case in
255 2015, there is no such compensation and BF_{ek} is different from 0 (see Fig. 4).

256 We now compare the accumulated B_{surf}^* from 1 September to 31 March the year after for the last
257 four deep convection years. It amounted to $-3.21 \times 10^9 \pm 0.05 \text{ J m}^{-2}$, $-2.29 \pm 0.04 \times 10^9 \text{ J m}^{-2}$, $-2.23 \pm$
258 $0.05 \times 10^9 \text{ J m}^{-2}$ and $-2.58 \pm 0.05 \times 10^9 \text{ J m}^{-2}$ for W2015, W2016, W2017 and W2018, respectively. The
259 cumulative sum of BF_{ek} from 1 September 2014 to 31 March 2015 was $-0.27 \pm 0.04 \times 10^9 \text{ J m}^{-2}$; the
260 estimates for the following winters were near 0 J m^{-2} . When the BF_{ek} is added to the B_{surf}^* , the
261 resulting atmospheric forcing is $-3.48 \times 10^9 \pm 0.05 \text{ J m}^{-2}$, $-2.19 \pm 0.04 \times 10^9 \text{ J m}^{-2}$, $-2.20 \pm 0.05 \times 10^9 \text{ J}$
262 m^{-2} and $-2.57 \pm 0.05 \times 10^9 \text{ J m}^{-2}$ for W2015, W2016, W2017 and W2018, respectively. The estimate
263 for W2015 is ~30% larger than the estimates for 2016 – 2018. Time series of atmospheric forcing
264 anomalies in Fig. 4 show that this strongly negative W2015 anomaly of accumulated B_{surf}^* was
265 caused by very negative Q and FWF anomalies and a negative BF_{ek} as well. During W2016, W2017
266 and W2018 however, all atmospheric forcing terms were close to zero.

267 From these results we conclude that, contrary to the very negative anomaly in atmospheric fluxes
268 over the Irminger Sea observed for W2015, the atmospheric fluxes were close to the mean during
269 W2016, W2017 and W2018.

270 4.3. Analysis of the preconditioning of the water column in the Irminger Sea

271 Our hypothesis is that the exceptional deep convection that happened in W2015 in the Irminger Sea
272 favorably preconditioned the water column for deep convection the following winters. The time-
273 evolution of θ , S, σ_1 and of $\Delta\sigma_1=0.01 \text{ kg m}^{-3}$ layer thicknesses (Fig. 5) show a marked change in the
274 hydrological properties of the Irminger Sea at the beginning of 2015 caused by the exceptional deep
275 convection that occurred during W2015 (see also Piron et al., 2017). The intermediate waters (500 –
276 1,000 m) became colder than the years before and, despite a slight decrease in salinity, the cooling
277 caused the density to increase (Fig. 5c). Fig. 5d shows $\Delta\sigma_1=0.01 \text{ kg m}^{-3}$ layer thicknesses larger than
278 600 m appearing at the end of W2015 for the first time since 2002. In the density range 32.36 – 32.39
279 kg m^{-3} , these layers remained thicker than ~450 m during W2016 to W2018. This indicates low



280 stratification at intermediate depths and a favorable preconditioning of intermediate waters for deep
281 convection due to W2015 deep convection.

282 $B(z_i)$ is our estimate of the preconditioning of the water column before winter (see Method). Fig. 6a
283 shows that, deeper than 100 m, B was smaller for W2016, W2017 and W2018 than for W2015 or for
284 the mean W2008 – W2014. Furthermore, for W2016, W2017 and 2018, B remained nearly constant
285 with depth between 600 and 1,300 m, which means that once the water column has been
286 homogenized down to 600 m, little additional buoyancy loss results in homogenization of the water
287 column down to 1,300 m. Both conditions (i) less buoyancy to be removed and (ii) absence of
288 gradient in the B profile down to 1,300 m indicate a more favorable preconditioning of the water
289 column for W2016, W2017 and W2018 than during W2008 – W2015.

290 To understand the relative contributions of θ and S to the preconditioning, we computed the thermal
291 (B_θ) and haline (B_s) components of B ($B = B_\theta + B_s$). In general, B_θ (B_s) increases with depth when θ
292 decreases (S increases) with depth. On the contrary, a negative slope in B_θ (B_s) corresponds to θ
293 increasing (S decreasing) with depth and is indicative of a destabilizing effect. The negative slopes in
294 B_θ and B_s profiles are not observed simultaneously because density profiles are stable.

295 We describe the relative contributions of B_θ and B_s to B by looking first at the mean 2008 – 2014
296 profiles (discontinuous blue lines in Fig. 6). B_θ accounts for most of the increase in B from the surface
297 to 800 m and below 1,400 m. The negative slope in the B_s profile between 800 – 1,000 slightly
298 reduces B and is due to the decrease in S associated with the core of LSW (see Fig. 3 in Piron et al.
299 2016). In the layer 1,000 – 1,400 m, the increase in B is mainly explained by B_s , which follows the
300 increase in S in the transition from LSW to Iceland Scotland Overflow Water (ISOW) that will be
301 referred to hereinafter as the deep halocline. The evaluation of the preconditioning of the water
302 column was usually analyzed in terms of heat (e.g., Piron et al. 2015; 2017). The decomposition of B
303 in B_θ and B_s reveals that θ governs B in the layer 0 – 800 m. S tends to reduce the stabilizing effect of
304 θ in the layer 800 – 1,000 m, and reinforces it in the layer 1,000 – 1,400 m in adding up to $1 \times 10^9 \text{ J m}^2$
305 to B .

306 In order to further understand why the Irminger Sea was favorably preconditioned during winters
307 2016 – 2018, we compare the B_θ and B_s of W2017, which was the most favorably preconditioned
308 winter, with the mean 2008 – 2014 (Fig. 7a). From the surface to 1,600 m, B_θ and B_s were smaller for
309 W2017 than for the mean 2008 – 2014. There are two additional remarkable features. First, in the
310 layer 500 – 1000 m, the large reduction of B_θ , in relation to its mean 2008 – 2014, mostly explains the
311 decrease of B in this layer. Second, the more negative value of B_s in the layer 1,100 – 1,300 m,
312 compared to its mean 2008 – 2014, eroded the B_θ slope, making the B profile more vertical for



313 W2017 than in the mean. The more negative contribution of B_s in the layer 1,100 – 1,300 m is related
314 to the fact that the deep halocline was deeper for W2017 (1,300 m, see red discontinuous line in Fig.
315 7a) than for the mean 2008 – 2014 (1,000 m, see blue discontinuous line in Fig. 7a). Finally, we note
316 that the profiles of $B(z_i)$, $B_0(z_i)$ and $B_s(z_i)$ for W2016 and W2018 are more similar to the profiles of
317 W2017 than to those of W2015 or to the mean 2008 – 2014 (see Fig. 6), which indicates that the
318 water column was also favorably preconditioned for deep convection in W2016 and W2018 for the
319 same reasons than in W2017.

320 The origin of the changes in B is now discussed from the evolution of the monthly anomalies of θ , S
321 and σ_0 at a point in the Irminger Sea (59°N – 40°W, Fig. 8). These anomalies were computed using
322 ISAS (Gaillard et al., 2016) and were referenced to the monthly mean of 2002 – 2016. A positive
323 anomaly of σ_0 appeared in 2015 between the surface and 600 m (Fig. 8a) and reached 1,100m in
324 2016 and beyond. This positive anomaly of σ_0 correlates with a negative anomaly of θ that, however,
325 reached ~1,400 m depth in 2016 that is deeper than the positive anomaly of σ_0 . The negative
326 anomaly of S between 1,000 - 1,500 m that started in 2016 caused the negative anomaly in σ_0
327 between 1,200 – 1,500 m (the negative anomaly in θ between 1,200 – 1,400 m does not balance the
328 negative anomaly of S).

329 The θ and S anomalies in the water column during 2016 – 2018 explain the anomalies of B , B_0 and B_s
330 and can be summarized as follows. On the one hand, the properties of the surface waters (down to
331 500 m) were colder than previous years and, despite they were also fresher, they were denser. The
332 density increase in the surface water reduced the density difference with the deeper-lying waters.
333 The intermediate layer (500 – 1000 m) was also favorably preconditioned due to the observed
334 cooling. Additionally, in the layer 1,100 – 1,300 m, the large negative contribution of B_s in relation to
335 its mean is explained by the decrease in S in this layer, which caused a decrease in σ_0 and,
336 consequently, reduced the σ_0 difference with the shallower-lying water. The decrease in S also
337 resulted in a deepening of the deep halocline.

338 4.4. Atmospheric forcing versus preconditioning of the water column

339 We now use the estimates of atmospheric forcing ($B_{\text{surf}}^* + BF_{\text{ek}}$) to predict the maximum convection
340 depth for a given winter based on September profiles of B . The predicted convection depths are
341 determined as the depth at which $B(z_i)$ equals the atmospheric forcing. The associated error was
342 estimated considering the error in the atmospheric forcing ($0.05 \times 10^9 \text{ J m}^{-2}$). We found predicted
343 convection depths of $1175 \pm 10 \text{ m}$, $1270 \pm 25 \text{ m}$, $1425 \pm 10 \text{ m}$ and $1285 \pm 20 \text{ m}$ for W2015, W2016,
344 W2017 and W2018, respectively. The Q3 estimated from W2016 and W2017 observations (1,325 m



345 and 1,400 m, respectively) are very close to the predicted convection depth. In W2015, the predicted
346 convection depth was underestimated compared to the observed Q3 (1,310 m). The contrary is
347 observed for W2018; this result is in line with the fact that Q3 in W2018 was most likely
348 underestimated since 6 out of the 10 profiles from which deep convection was recorded dived down
349 to 1,100 m, which coincided with their MLD. When these 6 profiles are excluded of the analysis, Q3 is
350 1,300 m, which is within the error bar of the predicted convection depth.

351 The satisfactory predictability of the convection depth validates our neglect of the horizontal
352 advection and indicates that deep convection occurred locally. Finally, this demonstrates that in spite
353 the atmospheric forcing was close to mean conditions during W2016, W2017 and W2018, convection
354 depths > 1300 m were reached, which was only possible thanks to the favorable preconditioning.

355

356 5. DISCUSSION

357 Deep convection happens in the Irminger Sea during specific winters because of strong atmospheric
358 forcing (high buoyancy loss), favorable preconditioning (low stratification) or both at the same time
359 (Pickart et al., 2003). Strong atmospheric forcing explained for instance the very deep convection
360 (reaching depth greater than 1500 m) observed in the early 90s (Pickart, et al., 2003) and in W2015
361 (de Jong et al. 2016; Piron et al. 2017), and the return of deep convection after many years without
362 convection in W2008 (Våge et al., 2009) and in W2012 (Piron et al., 2016). The favorable
363 preconditioning caused by the densification of the convected layer at the end of W2008 favored a
364 new deep convection event in W2009 despite neutral atmospheric forcing (de Jong et al. 2012).
365 Similarly, the preconditioning observed after W2015 favored deep convection in W2016 (this work).
366 Our study reveals that the preconditioning surprisingly persisted along three consecutive winters
367 (2016 – 2018) which allowed deep convection although atmospheric forcing was close to the
368 climatological values. Why did this favorable preconditioning persist in time?

369 The favorable preconditioning of the water column during 2016 – 2018 in the Irminger Sea resulted
370 from two hydrological anomalies affecting different ranges of the water column: the cooling of the
371 layer 200 – 800 m and the freshening of 1,200 – 1,400 m layer. Note that, the cooling affected the
372 layer surface – 1,400 m and the freshening affected the layer 1,000 – 1,500 m (Fig. 8), but the θ_S
373 anomalies were density compensated in the layer 1,000 – 1,200 m.

374 We see in Fig. 5a a sudden decrease in θ in the intermediate layers compared to the previous years.
375 It indicates that the decrease in θ of the layer 200 – 800 m likely originated locally during W2015
376 when extraordinary deep convection happened. The freshening of the layer 1,200 – 1,400 m
377 appeared in 2016 (Fig. 8c). Given its depth range, it is unlikely that this anomaly was locally formed.



378 Moreover, this anomaly is different to that affecting the intermediate layer because density
379 increased in the intermediate layer with respect to the mean 2002 – 2016, while it decreased in the
380 1,200 – 1,400 m layer (Fig. 8a). Our hypothesis is that the S anomaly originated in the Labrador Sea
381 and was further transferred to the Irminger Sea by the cyclonic circulation encompassing the
382 Labrador Sea and Irminger Sea at these depths (Daniault et al., 2016; Ollitrault & Colin de Verdière,
383 2014). It is corroborated by the 2D evolution of the anomalies in S in the layer 1,200 – 1,400 m (Fig.
384 9): a negative anomaly in S appeared in the Labrador Sea in February 2015, which was transferred
385 southward and northeastward in February 2016 and intensified over the whole SPNA in February
386 2017.

387 We now compare the atmospheric forcing and the preconditioning of the water column in the
388 Irminger Sea with those of the nearby Labrador Sea where deep convection happens each year. As
389 noted by Pickart et al. (2003), the atmospheric forcing over the Labrador Sea is ~15 % larger than that
390 over the Irminger Sea: the means (1993 - 2018) of the atmospheric forcing, defined as the time -
391 accumulated $B_{\text{surf}}^* + BF_{\text{ek}}$ from 1 September to 31 March the year after, are $-2.61 \pm 0.55 \times 10^9 \text{ J m}^{-2}$ in
392 the Labrador Sea and $-2.26 \pm 0.58 \times 10^9 \text{ J m}^{-2}$ in the Irminger Sea. The difference was larger during the
393 period 2016 – 2018 when the atmospheric forcing equaled $-3.10 \pm 0.19 \times 10^9 \text{ J m}^{-2}$ in the Labrador
394 Sea and $-2.31 \pm 0.21 \times 10^9 \text{ J m}^{-2}$ in the Irminger Sea. In terms of preconditioning, the 2008 – 2014
395 mean B profile (blue continuous lines in Fig. 7) was lower by $\sim 0.5 \times 10^9 \text{ J m}^{-2}$ in the Labrador Sea than
396 in the Irminger Sea for the surface to 1,000 m layer and by more than $1 \times 10^9 \text{ J m}^{-2}$ below 1,000 m. It
397 indicates that the water column was more favorably preconditioned in the Labrador Sea than in the
398 Irminger Sea. Differently, B for W2017 shows slightly lower values from the surface to 1,300 m in the
399 Irminger Sea than in the Labrador Sea (see orange lines in Fig. 7). However, B in the Labrador Sea
400 remains constant down to the depth of the deep halocline between LSW and North Atlantic Deep
401 Water (NADW) at 1,700 m. In the Irminger Sea, the deep halocline remained at $\sim 1,300 \text{ m}$ between
402 2016 and 2018 (see B_s lines in Fig. 7a). Differently, in the Labrador Sea, the deep halocline was
403 successive deepening from 1,200 m for the mean to 1,735 m, 1,775 m and 1905 m in W2016, W2017
404 and W2018, respectively (see discontinuous lines in Fig. 7b). The deep halocline acts as a physical
405 barrier for deep convection in both the Irminger Sea and the Labrador Sea, but because it is deeper
406 in the Labrador Sea than in the Irminger Sea, a deeper convection depth is granted in the former
407 than in the latter. Summarizing, the atmospheric forcing and the preconditioning of the water
408 column are in general more favorable for deep convection in the Labrador Sea than in the Irminger
409 Sea. In winters 2016 - 2018 in the Labrador Sea, both atmospheric forcing and preconditioning of the
410 water column favored by a deeper than average deep halocline, granted the deepest convection
411 depth ever observed in the Labrador Sea (comparison of our results with those of Yashayaev and



412 Loader, 2017). Contrasting, in the Irminger Sea, during the same period, the atmospheric forcing was
413 close to climatological values, and the favorable preconditioning of the water column allowed 1,300
414 m depth convection, what was exceptional for the Irminger Sea.

415 In the following we consider the time – evolution of θ , S and σ_0 at the layer 700 – 900 m (Fig. 10),
416 considered here as the core of the LSW in both the Irminger Sea and the Labrador Sea. From 2002 to
417 2012, a progressive increase in the θ and S of the LSW core in the Irminger Sea is noticeable despite
418 the high frequency variability. The θ and S changes were not density compensated causing a decadal
419 decrease in σ_0 of $\sim 0.01 \text{ Kg m}^{-3}$. From 2012 to 2015, both θ and S decreased, while σ_0 remained
420 constant. During 2015 – 2018, θ decreased from $3.6 \text{ }^\circ\text{C}$ to $3.2 \text{ }^\circ\text{C}$, and σ_0 increased from 27.72 to
421 27.75 kg m^{-3} (see also Fig. 3 and Table 1). In spite of the cooling and densification that occurred
422 during the last winters, LSW is warmer and lighter than that formed during W1994 and W1995
423 (2.85°C , 27.78 kg m^{-3} , Pickart et al. 2003). We note a long-term (1994 – 2018) warming of LSW
424 observed in the Irminger Sea. The comparison with the LSW properties in the Labrador Sea over 2002
425 – 2018 (Fig. 9) shows that the LSW observed in both basin has the same density while that of the
426 Irminger Sea is warmer and saltier than that of the Labrador Sea. Interestingly, this behaviour was
427 also observed along the 90s (Pickart et al, 2003). It is also worth noting that θ and S observed in
428 Labrador Sea and Irminger Sea converged at the end of the 90s (Fig. 6 in Pickart et al., 2003) and
429 along our period 2015 – 2018 (Fig. 3 and Fig. 10). However, there is an important difference between
430 the two periods: deep convection was not observed in the Irminger Sea at the end of the 90s while it
431 was very intense during 2015 – 2018. This disparity might indicate that Labrador Sea and Irminger
432 Sea are evolving differently and only further observations would disclose the origin and mechanisms
433 causing the differences.

434 Climate models forecast increasing input of freshwater in the North Atlantic due to ice-melting under
435 present climate change (Bramber et al., 2018), which could reduce, or even shut-down, the deep
436 convection in the North Atlantic (Yang et al., 2016; Brodeau & Koenigk, 2016). We observed a fresh
437 anomaly in the surface waters in regions close to the eastern coast of Greenland in 2016 that
438 extended to the whole Irminger Sea in 2017 (Fig. S4). However, at the moment, the surface
439 freshening did not hamper the deep convection in the Irminger Sea possibly because the surface
440 water also cooled, which favors the preconditioning for deep convection. Swingedouw et al., 2013
441 indicated that the freshwater signal due to Greenland ice sheet melting is mainly accumulating in the
442 Labrador Sea. However, no negative anomaly of S was detected in the surface waters of the Labrador
443 Sea (Fig. S4). It might be explained by the intense deep convection affecting the Labrador Sea since
444 2014 that could have transferred the surface freshwater anomaly to the ocean interior. This suggest



445 that, in the last years, the interactions between expected climate change anomalies and the natural
446 dynamics of the system combined to favor very deep convection. This however does not foretell the
447 long term response to climate change.

448

449 **6. CONCLUSIONS**

450 During 2015 – 2018 winter deep convection happened in the Irminger Sea reaching deeper than
451 1,300 m. It is the first time deep convection was observed in the Irminger Sea during four
452 consecutive winters. LSW formed in the Irminger Sea from 2015 to 2018 get colder, fresher and
453 denser, being similar in 2018 to the properties of the LSW formed in the Labrador Sea.

454 Considering the expected increase in freshwater inputs, the atmospheric forcing and preconditioning
455 of the water column was evaluated in terms of buoyancy. We showed that the atmospheric forcing is
456 10% weaker when evaluated in terms of buoyancy than in terms of heat because of the non-
457 negligible effect of the freshwater flux. The analysis of the preconditioning of the water column in
458 terms of buoyancy to be removed (B) and its thermal and salinity terms (B_θ and B_s) revealed that B_θ
459 dominated the B profile from the surface to 800 m and B_s reduced the B in the 800 – 1000 m layer
460 because of low salinity of LSW. Deeper, B_s increased B due to the deep halocline (LSW-ISOW) that
461 acted as a physical barrier limiting the depth of the convection.

462 During 2016 – 2018, the air-sea buoyancy losses were close to the climatological values and the very
463 deep convection was possible thanks to the favorable preconditioning of the water column. It was
464 surprising that these events reached convection depths similar to those observed in W2012 and
465 W2015, when the latter were provoked by high air-sea buoyancy loss intensified by the effect of
466 strong wind stress. It was also surprising that the water column remained favorably preconditioned
467 during three consecutive winters without strong atmospheric forcing. In this paper, we studied the
468 reasons why this happened.

469 The favorable preconditioning for deep convection during 2016 – 2018 was due to the combination
470 of two types of hydrological anomalies affecting different depth ranges. First, the intermediate water
471 (200 – 800 m) was favorably preconditioned because buoyancy (density) decreased (increased) due
472 to the cooling caused by the deep convection of W2015. Second, buoyancy (density) increased
473 (decreased) in the layer 1,200 – 1,400 m due to the decrease in S caused by the lateral advection of
474 fresher LSW formed in the Labrador Sea. The S anomaly of this layer resulted in a deeper deep
475 halocline. Hence, the cooling of the intermediate water was essential to reach convection depth of



476 800 – 1,000 m, and the freshening in the layer 1,200 – 1,400 m and the associated deepening of the
477 deep halocline, allowed the very deep convection (> 1,300 m) in W2016 – W2018.

478 **Author contribution:** PZ treated and analyzed the data. PZ and HM interpreted the results. PZ, HM
479 and VT discussed the results and wrote the paper.

480

481 **ACKNOWLEDGEMENT**

482 The Argo data were collected and made freely available by the International Argo Program and the
483 national programs that contribute to
484 it. (<http://www.argo.ucsd.edu>, <http://argo.jcommops.org>). The Argo Program is part of the Global
485 Ocean Observing System. The NAO data were downloaded from the UCAR Climate Data Guide
486 website (Schneider et al., 2013): [https://climatedataguide.ucar.edu/climate-data/hurrell-north-
487 atlantic-oscillation-nao-index-pc-based](https://climatedataguide.ucar.edu/climate-data/hurrell-north-atlantic-oscillation-nao-index-pc-based). The Ssalto/Duacs altimeter products were produced and
488 distributed by the Copernicus Marine and Environment Monitoring Service (CMEMS)
489 (<http://www.marine.copernicus.eu>).

490

491 **REFERENCES**

- 492 Argo Data Management Team: Argo user’s manual V3.2. <https://doi.org/10.13155/29825>, 2017
- 493 Argo group: Argo float data and metadata from Global Data Assembly Centre (Argo GDAC),
494 SEANOE, https://doi.org/10.17882/42182_2019
- 495 Bacon, S.: Circulation and Fluxes in the North Atlantic between Greenland and Ireland. *Journal of*
496 *Physical Oceanography*, 27(7), 1420–1435. [https://doi.org/10.1175/1520-
497 0485\(1997\)027<1420:CAFITN>2.0.CO;2](https://doi.org/10.1175/1520-0485(1997)027<1420:CAFITN>2.0.CO;2), 1997.
- 498 Bamber, J. L., Tedstone, A. J., King, M. D., Howat, I. M., Enderlin, E. M., van den Broeke, M. R., & Noel,
499 B.: Land Ice Freshwater Budget of the Arctic and North Atlantic Oceans: 1. Data, Methods, and
500 Results, *Journal of Geophysical Research: Oceans*, 1–11,
501 <https://doi.org/10.1002/2017JC013605>, 2018.
- 502 Billheimer, S., & Talley, L. D.: Near cessation of Eighteen Degree Water renewal in the western North
503 Atlantic in the warm winter of 2011 – 2012, *118*(November), 6838–6853,
504 <https://doi.org/10.1002/2013JC009024>, 2013.



- 505 Brodeau, L., & Koenigk, T.: Extinction of the northern oceanic deep convection in an ensemble of
506 climate model simulations of the 20th and 21st centuries, *Climate Dynamics*, 46(9–10), 2863–
507 2882. <https://doi.org/10.1007/s00382-015-2736-5>, 2016.
- 508 Centurioni and Gould, W. J.: Winter conditions in the Irminger Sea observed with profiling floats,
509 *Journal of Marine Research*, 62, 313–336, 2004.
- 510 Danialt, N., Mercier, H., Lherminier, P., Sarafanov, A., Falina, A., Zunino, P., Gladyshev, S. : The
511 northern North Atlantic Ocean mean circulation in the early 21st century, *Progress in*
512 *Oceanography*, 146(June), 142–158, <https://doi.org/10.1016/j.pocean.2016.06.007>, 2016.
- 513 de Boyer Montégut, C., Madec, G., Fischer, A. S., Lazar, A., & Iudicone, D.: Mixed layer depth over the
514 global ocean: An examination of profile data and a profile-based climatology, *Journal of*
515 *Geophysical Research C: Oceans*, 109(12), 1–20, <https://doi.org/10.1029/2004JC002378>, 2004.
- 516 de Jong, M.F., Oltmanns, M., Karstensen, J., and de Steur, L.: Deep Convection in the Irminger Sea
517 Observed with a Dense Mooring Array, 31(February), 50–59,
518 <https://doi.org/10.5670/oceanog.2018.109>, 2018.
- 519 de Jong, M. F., & de Steur, L.: Strong winter cooling over the Irminger Sea in winter 2014–2015,
520 exceptional deep convection, and the emergence of anomalously low SST, *Geophysical*
521 *Research Letters*, 43(13), 7106–7113. <https://doi.org/10.1002/2016GL069596>, 2016.
- 522 De Jong, M. F., Van Aken, H. M., Våge, K., & Pickart, R. S.: Convective mixing in the central Irminger
523 Sea: 2002-2010, *Deep-Sea Research Part I: Oceanographic Research Papers*, 63, 36–51.
524 <https://doi.org/10.1016/j.dsr.2012.01.003>, 2012.
- 525 Dee, D. P., Uppala, S. M., Simmons, A. J., Berrisford, P., Poli, P., Kobayashi, S., Vitart, F.: The ERA-
526 Interim reanalysis: Configuration and performance of the data assimilation system, *Quarterly*
527 *Journal of the Royal Meteorological Society*, 137(656), 553–597. <https://doi.org/10.1002/qj.828>,
528 2011.
- 529 Gaillard, F., Reynaud, T., Thierry, V., Kolodziejczyk, N., & Von Schuckmann, K.: In situ-based reanalysis
530 of the global ocean temperature and salinity with ISAS: Variability of the heat content and steric
531 height. *Journal of Climate*, 29(4), 1305–1323. <https://doi.org/10.1175/JCLI-D-15-0028.1>, 2016.
- 532 Good, S. A., Martin, M. J., & Rayner, N. A.: EN4: Quality controlled ocean temperature and salinity
533 profiles and monthly objective analyses with uncertainty estimates. *Journal of Geophysical*
534 *Research: Oceans*, 118(12), 6704–6716. <https://doi.org/10.1002/2013JC009067>, 2013.



- 535 IPCC: Climate Change 2013: The Physical Science Basis. Contribution of Working Group I to the Fifth
536 Assessment Report of the Intergovernmental Panel on Climate Change [Stocker, T.F., D. Qin, G.-
537 K. Plattner, M. Tignor, S.K. Allen, J. Boschung, A. Nauels, Y. Xia, V. Bex and P.M. Midgley (eds.)].
538 Cambridge University Press, Cambridge, United Kingdom and New York, NY, USA, 1535 pp,
539 2013.
- 540 Kieke, D., & Yashayaev, I.: Studies of Labrador Sea Water formation and variability in the subpolar
541 North Atlantic in the light of international partnership and collaboration. *Progress in*
542 *Oceanography*, 132, 220–232. <https://doi.org/10.1016/j.pocean.2014.12.010>, 2015a.
- 543 Kieke, D., & Yashayaev, I.: Studies of Labrador Sea Water formation and variability in the subpolar
544 North Atlantic in the light of international partnership and collaboration, *Progress in*
545 *Oceanography*, 132, 220–232, <https://doi.org/10.1016/j.pocean.2014.12.010>, 2015b.
- 546 Kolodziejczyk, N., Prigent-Mazella A., and Gaillard F. (2017). ISAS-15 temperature and salinity gridded
547 fields. **SEANOE**. <http://doi.org/10.17882/52367>
- 548 Marshall, J., & Schott, F.: Open-Ocean Convection ' Theory , and Models Observations ,. *Reviews of*
549 *Geophysics*, 37(98), 1–64. <https://doi.org/10.1029/98RG02739>, 1999.
- 550 Ollitruault, M., & Colin de Verdière, A.: The Ocean General Circulation near 1000-m Depth, *Journal of*
551 *Physical Oceanography*, 44(1), 384–409. <https://doi.org/10.1175/JPO-D-13-030.1>, 2014.
- 552 Pickart, R. S., Straneo, F., & Moore, G. W. K.: Is Labrador Sea Water formed in the Irminger basin?
553 *Deep-Sea Research Part I: Oceanographic Research Papers*, 50(1), 23–52,
554 [https://doi.org/10.1016/S0967-0637\(02\)00134-6](https://doi.org/10.1016/S0967-0637(02)00134-6), 2003.
- 555 Piron, A., Thierry, V., Mercier, H., & Caniaux, G.: Argo float observations of basin-scale deep
556 convection in the Irminger sea during winter 2011–2012. *Deep-Sea Research Part I:*
557 *Oceanographic Research Papers*, 109, 76–90. <https://doi.org/10.1016/j.dsr.2015.12.012>, 2016.
- 558 Piron, A., Thierry, V., Mercier, H., & Caniaux, G.: Gyre-scale deep convection in the subpolar North
559 Atlantic Ocean during winter 2014–2015. *Geophysical Research Letters*, 44(3), 1439–1447.
560 <https://doi.org/10.1002/2016GL071895>, 2017.
- 561 Rahmstorf, S., Box, J. E., Feulner, G., Mann, M. E., Robinson, A., Rutherford, S., & Schaffernicht, E. J.:
562 Exceptional twentieth-century slowdown in Atlantic Ocean overturning circulation, *Nature*
563 *Climate Change*, 5(5), 475–480. <https://doi.org/10.1038/nclimate2554>, 2015.
- 564 Rhein, M, Steinfeldt, R, Kieke, D, Stendardo, I and Yashayaev, I.: Ventilation variability of Labrador



- 565 Sea Water and its impact on oxygen and anthropogenic carbon: a review, *Philosophical*
566 *Transactions of the Royal Society A: Mathematical, Physical and Engineering Sciences*,
567 375(2102). 20160321. [doi:10.1098/rsta.2016.0321](https://doi.org/10.1098/rsta.2016.0321), 2017.
- 568 Schmidt, S., & Send, U.: Origin and Composition of Seasonal Labrador Sea Freshwater, *Journal of*
569 *Physical Oceanography*, 37(6), 1445–1454. <https://doi.org/10.1175/JPO3065.1>, 2007.
- 570 Swingedouw, D., Rodehacke, C. B., Behrens, E., Menary, M., Olsen, S. M., & Gao, Y.: Decadal
571 fingerprints of freshwater discharge around Greenland in a multi-model ensemble, 695–720.
572 <https://doi.org/10.1007/s00382-012-1479-9>, 2013.
- 573 Thomson, R. E., & Fine, I. V.: Estimating mixed layer depth from oceanic profile data, *Journal of*
574 *Atmospheric and Oceanic Technology*, 20(2), 319–329. [https://doi.org/10.1175/1520-0426\(2003\)020<0319:EMLDFO>2.0.CO;2](https://doi.org/10.1175/1520-0426(2003)020<0319:EMLDFO>2.0.CO;2), 2003.
- 576 Yang, Q., Dixon, T. H., Myers, P. G., Bonin, J., Chambers, D., & Van Den Broeke, M. R.: Recent
577 increases in Arctic freshwater flux affects Labrador Sea convection and Atlantic overturning
578 circulation, *Nature Communications*, 7, 1–7. <https://doi.org/10.1038/ncomms10525>, 2016.
- 579 Yashayaev, I., Bersch, M., & van Aken, H. M.: Spreading of the Labrador Sea Water to the Irminger
580 and Iceland basins, *Geophysical Research Letters*, 34(10), 1–8.
581 <https://doi.org/10.1029/2006GL028999>, 2007.
- 582 Yashayaev, I., & Clarke, A.: Evolution of North Atlantic Water Masses Inferred From Labrador Sea
583 Salinity Series, *Oceanography*, 21(1), 30–45. <https://doi.org/10.5670/oceanog.2008.65>, 2008.
- 584 Yashayaev, I., & Loder, J. W.: Recurrent replenishment of Labrador Sea Water and associated
585 decadal-scale variability, *Journal Geophysical Research: Oceans*, 121, 8095–8114,
586 <https://doi.org/10.1002/2016JC012046>, 2016.
- 587 Yashayaev, I., & Loder, J. W.: Further intensification of deep convection in the Labrador Sea in 2016.
588 *Geophysical Research Letters*, 44(3), 1429–1438. <https://doi.org/10.1002/2016GL071668>, 2017.
- 589 Zunino, P., Lherminier, P., Mercier, H., Daniault, N., García-Ibáñez, M. I., & Pérez, F. F.: The GEOVIDE
590 cruise in May-June 2014 reveals an intense Meridional Overturning Circulation over a cold and
591 fresh subpolar North Atlantic, *Biogeosciences*, 14(23), 5323–5342. <https://doi.org/10.5194/bg-14-5323-2017>, 2017.

593



594 Table 1. Properties of the deep convection in the Irminger Sea and in the Labrador Sea in winters
 595 2015 – 2018. We show: the maximal MLD observed, the aggregate maximum depth of convection
 596 Q3, the σ_0 , θ and S of the winter mixed layer formed during the convection event and n, which is the
 597 number of Argo profiles indicating deep convection. The uncertainties given with σ_0 , θ and S are the
 598 standard deviation of the n values considered to estimate the mean values.
 599

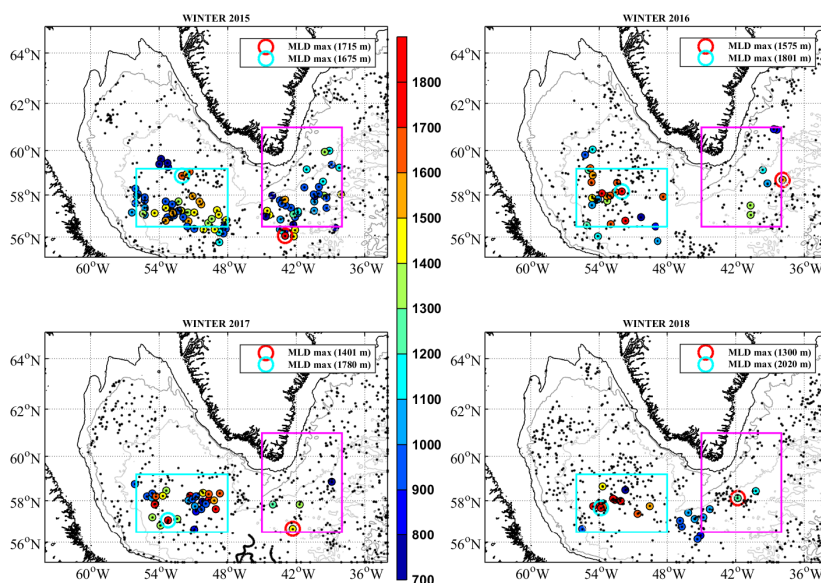
IRMINGER SEA	Maximal MLD	Q3 MLD	σ_0	θ	Salinity	n
W2015	1715	1310	27.732 ± 0.007	3.494 ± 0.139	34.868 ± 0.015	37
W2016	1575	1325	27.745 ± 0.004	3.444 ± 0.150	34.877 ±0.017	7
W2017	1400	1400	27.746 ± 0.006	3.324 ± 0.113	34.864 ± 0.009	4
W2018	1300	1100/1300*	27.751 ± 0.007	3.188 ± 0.058	34.854 ± 0.013	10
LABRADOR SEA	Maximal MLD	Q3 MLD	σ_0	θ	Salinity	n
W2015	1675	1504	27.733 ± 0.009	3.279 ± 0.036	34.842 ± 0.010	41
W2016	1801	1620	27.743 ± 0.006	3.124 ± 0.047	34.836 ± 0.010	18
W2017	1780	1674	27.752 ± 0.008	3.172 ± 0.029	34.853 ± 0.009	26
W2018	2020	1866	27.756 ± 0.006	3.145 ± 0.083	34.855 ± 0.010	13

600 *Q3 estimated when the data of Float 5903102 were excluded of the analysis. We exclude them
 601 because their MLDs matched with the maximal depth dived by the float.

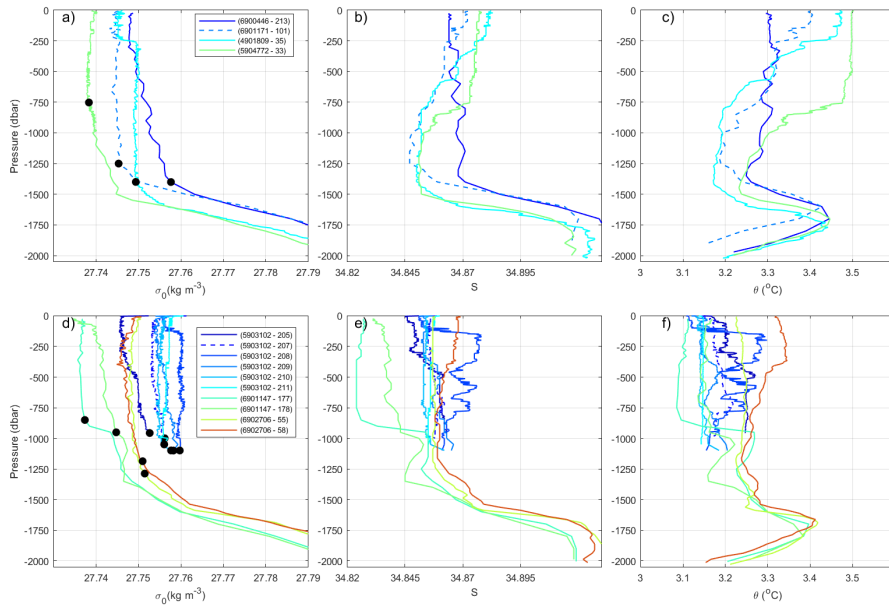
602
 603
 604



605 FIGURES



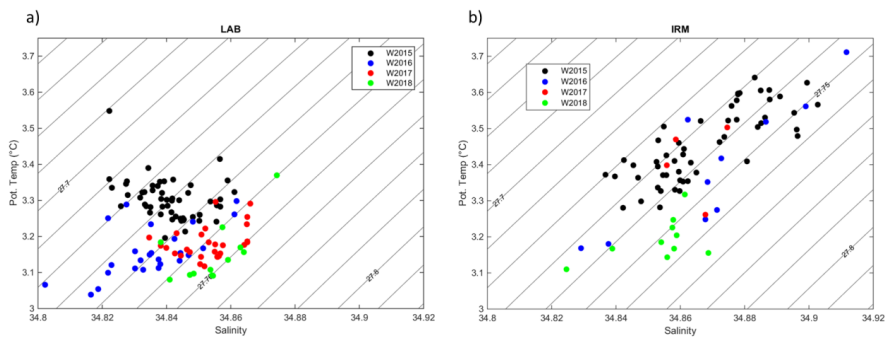
606
607 **Figure 1.** Position of all Argo floats north of 55°N in the Atlantic between 1 January and 30 April a)
608 2015, b) 2016, c) 2017 and d) 2018 (small black points). The colored big points and colorbar indicate
609 the depth of the mixed layer depth (MLD) when MLD deeper than 700 m, which indicates deep
610 convection. The circles correspond to the positions of the profiles with the maximum MLD for the
611 given box. The pink and cyan boxes delimit the regions used for estimating the time series of
612 atmospheric forcing and the vertical profiles of buoyancy to be removed in the Irminger Sea and
613 Labrador Sea, respectively (Irminger Sea: 56.5°N – 61.0°N and 45.0°W – 38.0°W, Labrador Sea:
614 56.5°N – 59.2°N and 56°W – 48°W).



615

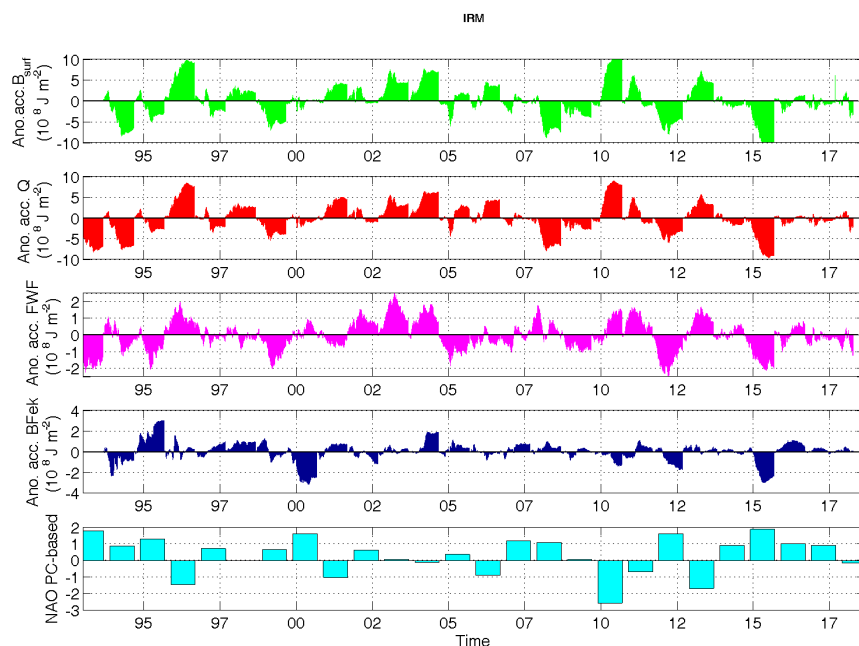
616 **Figure 2.** Vertical distribution of σ_0 , S and θ of Argo profiles showing MLD deeper than 700 m in the
 617 Irminger Sea in Winter 2017 (a, b and c) and in Winter 2018 (d, e, f). The black points indicate the
 618 MLD in each profile. In the legend, the float and cycle of each profile are indicated.

619

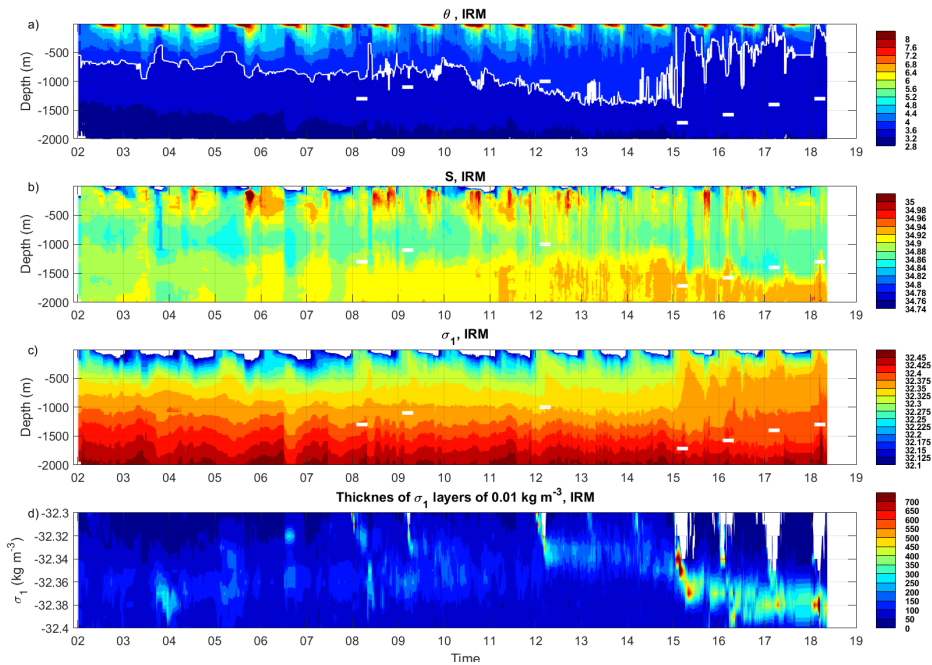


620

621 **Figure 3.** Diagram TS of the n profiles with MLD deeper than 700 m found a) in the Labrador Sea and
 622 b) in Irminger Sea, in the winters 2015, 2016, 2017 and 2018. The properties of each profile were
 623 estimated as the vertical mean between 200 m and the MLD.

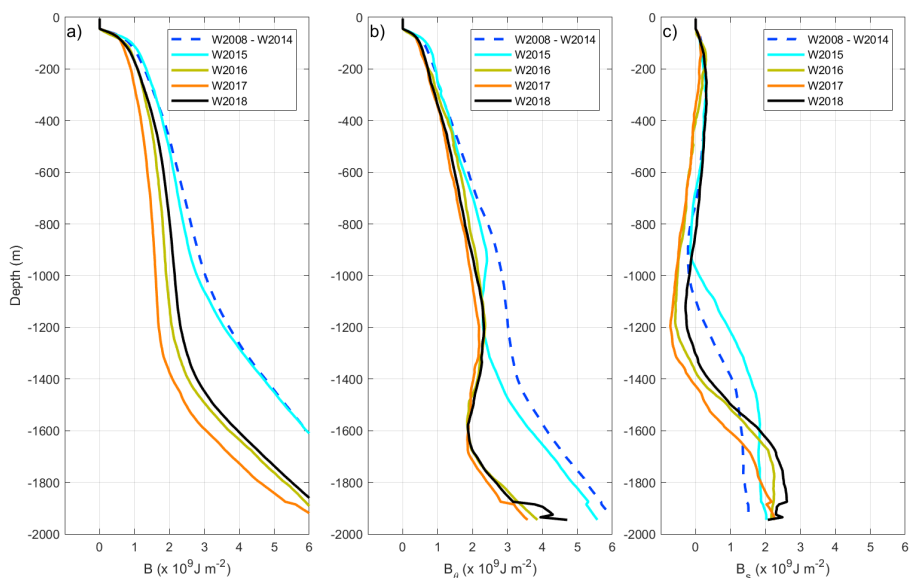


624
625 **Figure 4.** Time series of anomalies of accumulated B_{surf}^* , Q , FWF^* and B_{Fe_k} , averaged in the Irminger
626 Sea. They are anomalies with respect to 1993 – 2016. The accumulation was from 1 September to 31
627 August the following year. The winter NAO index (Hurrell et al., 2018) is also represented in the
628 bottom panel.



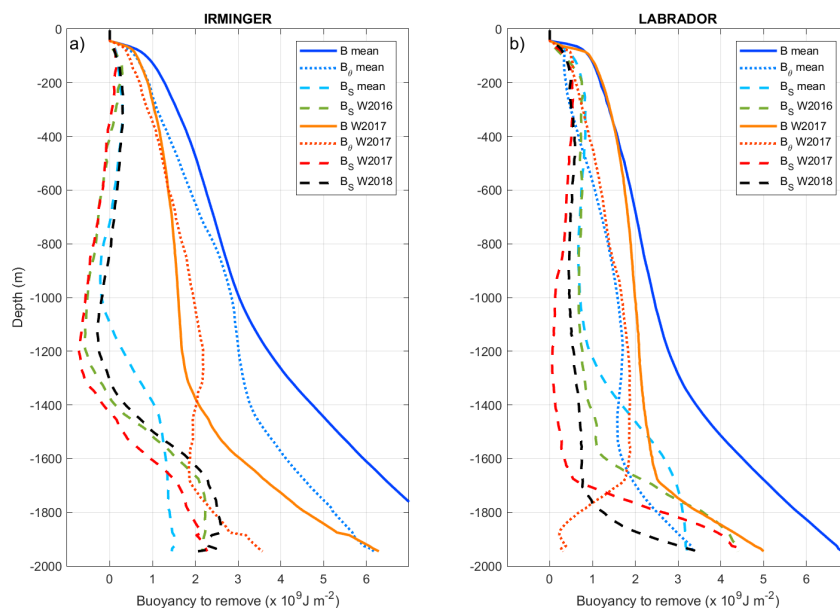
629
 630 **Figure 5.** Time-evolution of vertical profiles measured from Argo floats in the Irminger Sea: a) θ ; b) S;
 631 c) σ_1 and d) thickness of 0.01 kg m^{-3} thick σ_1 layers. The white horizontal bars in plots a), b) and c)
 632 indicate the maximal convection depth observed in the Irminger Sea when deep convection occurred. The white line in plot a) indicates the depth of the isotherm $3.6 \text{ }^\circ\text{C}$. These figures were
 634 created from all Argo profiles reaching deeper than 1000 m in the IRM region ($56.5^\circ - 61^\circ\text{N}$, $45^\circ -$
 635 38°W , pink box in Fig. 1). The yearly numbers of Argo profiles used in this figure are shown in Fig. S1.

636



637

638 **Figure 6.** Vertical profile of a) the total buoyancy to be removed (B), b) the thermal component (B_θ)
639 and c) the salinity component (B_s). They were calculated from Argo data measured in the Irminger
640 box (see Fig. 1) in September before the winter indicated in the legend. For W2018, we considered
641 data from 15/08/2017 to 30/09/2017 because not enough data were available in September 2017.
642 The number of Argo profiles taken into account to estimate the B profiles was more than ten for all
643 the winters.

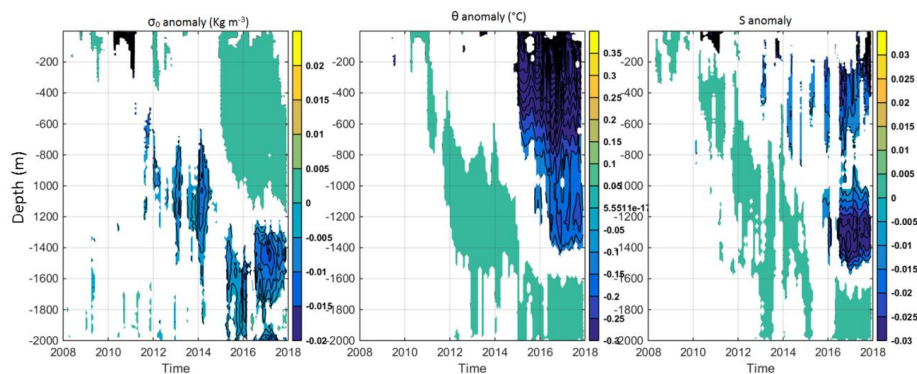


644

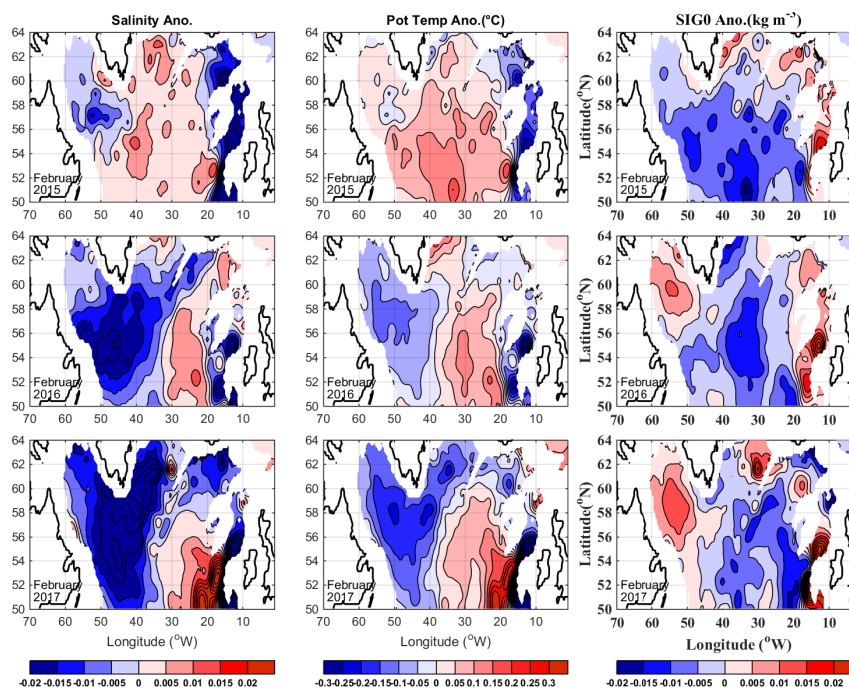
645 Figure 7. Decomposition of profiles of Buoyancy to be removed (B , continuous lines) in its thermal
646 (B_{θ} , point lines) and salinity (B_s , discontinuous lines) components in a) the Irminger Sea; b) the
647 Labrador Sea. To compare the mean 2008 – 2014 with W2017 compare reddish lines with bluish
648 lines. The B_s component in W2016 and W2018 was added in order to show the evolution of the
649 depth of the deep halocline in both the Irminger Sea and the Labrador Sea.

650

651

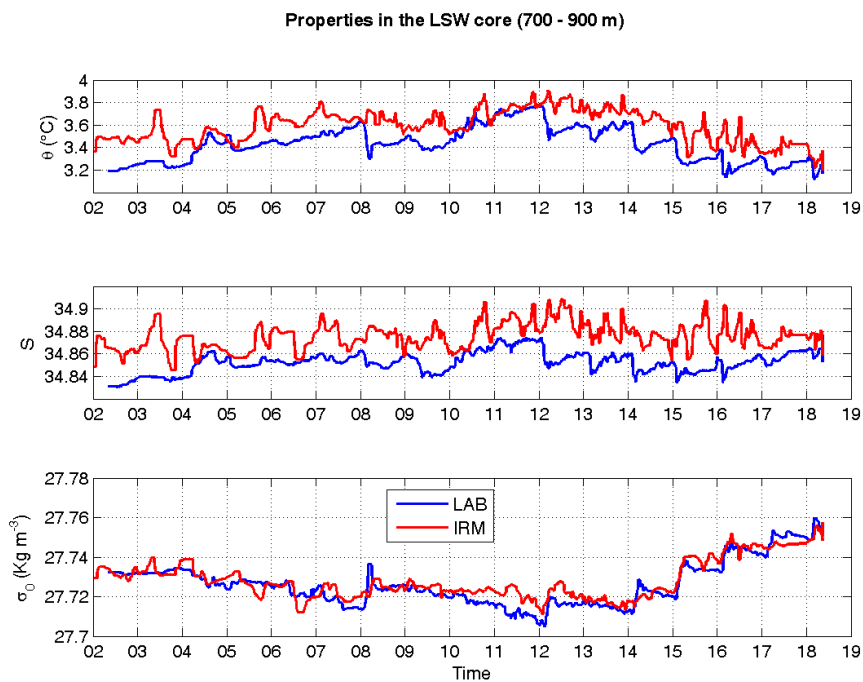


652
653 **Figure 8.** Evolution of vertical profiles of monthly anomalies of σ_0 (left panel), θ (central panel) and S
654 (right panel), at 59°N, 40°W in the Irminger Sea. The anomalies were estimated from the ISAS
655 database (Gaillard et al., 2016), they were referenced to the monthly mean estimated for 2002 –
656 2016. We represented only anomalies larger than one standard deviation of the mean and since
657 2008 in order to see clearly the recent changes. All anomalies are displayed in Fig. S3.



658
659 **Figure 9.** Horizontal distribution of the anomalies of S (left panels), θ (central panels) and σ_0 (right
660 panels) in the layer 1200 – 1400 m in February 2015 (upper panels), February 2016 (central panels)
661 and February 2017 (lower panels). The monthly anomalies were estimated from ISAS database
662 referenced to the period 2002 – 2016.

663



664

665 Figure 10. Time-evolution of the properties of the LSW core (700 – 900 m) in the Irminger Sea (red)
666 and Labrador Sea (blue), estimated from all Argo data in the pink and cyan boxes in Fig. 1.

667

668

669

670

671

672